Earth and Planetary Science Letters 491 (2018) 193–206

Contents lists available at ScienceDirect

Earth and Planetary Science Letters

www.elsevier.com/locate/epsl

Controls on the rheological properties of peridotite at a palaeosubduction interface: A transect across the base of the Oman–UAE ophiolite

Tyler K. Ambrose [a,*,1], David Wallis [a,b], Lars N. Hansen [a], Dave J. Waters [a,c], Michael P. Searle [a]

[a] University of Oxford, South Parks Road, Oxford, United Kingdom
[b] Department of Earth Sciences, Utrecht University, Utrecht, 3584 CD, Netherlands
[c] University Museum of Natural History, Parks Rd, Oxford OX1 3PW, United Kingdom

ARTICLE INFO

Article history:
Received 23 October 2017
Received in revised form 28 February 2018
Accepted 14 March 2018
Available online xxxx
Editor: J. Brodholt

Keywords:
plate boundary
strain localisation
olivine microstructure
Oman–UAE ophiolite
phase mixing
mantle wedge

ABSTRACT

Studies of experimentally deformed rocks and small-scale natural shear zones have demonstrated that volumetrically minor phases can control strain localisation by limiting grain growth and promoting grain-size sensitive deformation mechanisms. These small-scale studies are often used to infer a critical role for minor phases in the development of plate boundaries. However, the role of minor phases in strain localisation at an actual plate boundary remains to be tested by direct observation. In order to test the hypothesis that minor phases control strain localisation at plate boundaries, we conducted microstructural analyses of peridotite samples collected along a ~1 km transect across the base of the Oman-United Arab Emirates (UAE) ophiolite. The base of the ophiolite is marked by the Semail thrust, which represents the now exhumed contact between subducted oceanic crust and the overlying mantle wedge. As such, the base of the ophiolite provides the opportunity to directly examine a former plate boundary.

Our results demonstrate that the mean olivine grain size is inversely proportional to the abundance of minor phases (primarily orthopyroxene, as well as clinopyroxene, hornblende, and spinel), consistent with suppression of grain growth by grain-boundary pinning. Our results also reveal that mean olivine grain size is proportional to CPO strength (both of which generally decrease towards the metamorphic sole), suggesting that the fraction of strain produced by different deformation mechanisms varied spatially. Experimentally-derived flow laws indicate that under the inferred deformation conditions, the viscosity of olivine was grain-size sensitive. As such, grain size, and thereby the abundance of minor phases, influenced viscosity during subduction-related deformation along the base of the mantle wedge.

We calculate an order of magnitude decrease in the viscosity of olivine towards the base of the ophiolite, which suggests strain was localised near the subduction interface. Our data indicate that this rheological weakening was primarily the result of more abundant minor phases near the base of the ophiolite. Our interpretations are consistent with those of previous studies on experimentally deformed rocks and smaller-scale natural shear zones that indicate minor phases can exert the primary control on strain localisation. However, our study demonstrates for the first time that minor phases can control strain localisation at the scales relevant to a major plate boundary.

1. Introduction

Earth's lithosphere consists of highly viscous tectonic plates with deformation localised within less viscous material at plate boundaries (e.g., Bercovici and Karato, 2003). However, the processes that control the development of *plate boundary-scale* shear zones remain poorly constrained. Generating strain localisation in plate-tectonic models has proven challenging, primarily due to a lack of clarity on the best rheological parameterisation (e.g. Tackley, 2000). An often proposed mechanism for localised weakening is localised grain-size reduction, as exemplified by the occurrence of mylonites in ductile shear zones (e.g., Rutter and Brodie, 1988). Studies of small-scale natural shear zones (Hansen and Warren, 2015; Herwegh et al., 2011; Toy et al., 2010;

* Corresponding author.
E-mail address: tambrose@eoas.ubc.ca (T.K. Ambrose).
[1] Present address: Department of Earth, Ocean and Atmospheric Sciences, The University of British Columbia, Vancouver, British Columbia, V6T 1Z4, Canada.

https://doi.org/10.1016/j.epsl.2018.03.027
0012-821X/

Warren and Hirth, 2006) and experimentally deformed rocks (Farla et al., 2013; Hiraga et al., 2010) have demonstrated that volumetrically minor phases in polyphase rocks can control strain localisation by limiting grain-growth, enhancing and maintaining grain-size reduction, and thereby promoting grain-size sensitive creep. Theoretical models of grain-size evolution in polyphase rocks have suggested that, via this positive self-weakening feedback, minor phases play a fundamental role in the development and long-term maintenance of weak plate boundaries (e.g., Bercovici and Skemer, 2017; Mulyukova and Bercovici, 2017).

During shearing, increased intracrystalline strain drives dynamic recrystallisation and grain-size reduction (e.g., Poirier and Guillopé, 1979). Sufficient grain-size reduction can promote grain-size sensitive deformation mechanisms and associated rheological weakening (e.g., Drury, 2005). However, grain-size reduction is opposed by surface energy-driven grain growth, which increases with decreasing grain size (de Bresser et al., 1998, 2001). The steady state grain size depends on the relative contributions of grain-size reduction and grain growth (Austin and Evans, 2009; Derby and Ashby, 1987). In monophase rocks, the resulting equilibrium grain size tends to fall near the transition between the dislocation creep and diffusion creep fields, thus limiting the magnitude of rheological weakening possible through increased activity of grain-size sensitive deformation mechanisms (de Bresser et al., 1998, 2001). In polyphase rocks, however, an even finer grain size can be maintained by a well-mixed (i.e., dispersed) minor phase that pins grain boundaries, limiting grain-boundary migration and grain growth (e.g., Toy et al., 2010; Cross and Skemer, 2017). As such, by promoting and maintaining a finer grain size than would be expected in a monophase rock at a given stress, the presence of minor phases appears critical in promoting grain-size sensitive deformation and thus the dynamic rheological weakening necessary for strain localisation. This concept has been successfully implemented in analyses of plate boundary formation and stability with encouraging results (Bercovici and Ricard, 2012, 2014). However, while observations of the role of minor phases in strain localisation have been made from the thin-section to the outcrop scale, it remains to be tested with direct observation whether this process is applicable to strain localisation at an actual plate boundary.

Here we test the hypothesis that minor phases control strain localisation at plate boundaries by examining mantle rocks at a palaeosubduction interface. We analysed peridotite samples collected across a basal section of the Oman-United Arab Emirates (UAE) ophiolite. The ophiolite formed above a subduction zone during the late Cretaceous (MacLeod et al., 2013; Pearce et al., 1981; Rioux et al., 2016). The base of the ophiolite is bound by the Semail thrust, which represents the fossilised contact between subducted Tethyan crust and overlying mantle wedge (e.g., Searle and Malpas, 1980; Searle and Malpas, 1982; Cowan et al., 2014). Whereas previous studies have had to extrapolate data from experiments or natural shear zones of a small scale and/or uncertain tectonic context, the Semail thrust provides the opportunity to directly examine a former plate boundary. We used electron backscatter diffraction (EBSD) to quantify trends and relationships in grain size, modal mineral abundance, and crystallographic preferred orientation (CPO). Our results support microstructural and rheological models in which minor phases hinder olivine grain growth, which promotes diffusion creep, and thereby strongly influences strain localisation at plate boundaries.

2. Geologic setting

The Oman–UAE ophiolite (Fig. 1) is a thrust-bound slice of oceanic lithosphere formed at *ca*. 96.4–95.5 Ma in the hanging wall of a newly initiated, northeast dipping, intraoceanic subduction zone (Pearce et al., 1981; Rioux et al., 2012, 2013, 2016; Macleod et al., 2013). The ophiolite consists of upper-mantle peridotite overlain by a crustal section of gabbros, sheeted dykes, basaltic flows and pillows, and pelagic sediments (e.g., Glennie et al., 1973). Following subduction initiation, tholeiitic basalts, gabbros, and sediments were subducted beneath the newly forming ophiolite to form the metamorphic sole (Searle and Malpas, 1980, 1982; Gnos, 1998; Cowan et al., 2014). Burial, accretion to the base of the ophiolite, and the onset of exhumation of the sole occurred within about one million years of subduction initiation (Hacker, 1994; Rioux et al., 2016). Following exhumation of the sole, deformation stepped to shallower levels in the foreland as convergence was accommodated by in-sequence stacking of rise, slope, and shelf sedimentary packages (e.g.; Searle, 1988). By *ca*. 79 Ma, the continental margin reached the subduction zone and was subducted to eclogite facies in the southeastern part of the ophiolite in Oman (Warren et al., 2005). The obduction process was complete by ∼70 Ma and is marked by the return of shallow-marine passive margin sedimentation (Glennie et al., 1973).

For the most part, the mantle section of the ophiolite does not exhibit any obvious structure (Fig. 2a). However, the basal few hundred metres of the ophiolite exhibits a mylonitic fabric, with grain size that is smaller and foliation that is more pronounced towards the base of the ophiolite (Figs. 2b–d). The base of the ophiolite is marked by the Semail thrust, which placed the ophiolite over the metamorphic sole, a thrust slice of highly sheared amphibolite, quartz schist, and metachert that was scraped off the downgoing slab and accreted to the base of the mantle wedge (Fig. 1).

Several structural and petrological characteristics suggest that the mylonitic fabric in the peridotites adjacent to the Semail thrust is related to the early high-temperature history of subduction. (1) Deformation was ductile and distributed over hundreds of meters. (2) In addition to olivine and orthopyroxene, the mylonitic peridotites also contain clinopyroxene and hornblende, which have previously been interpreted to be related to fluids released from the downgoing slab (Prigent et al., 2014, 2015). Microstructural evidence (discussed in more detail in Section 4.1) indicates that these phases were present during deformation at temperatures in excess of 650 °C. (3) Although the mineral assemblage of the peridotites is not suitable for thermobarometry, thermobarometric estimates for garnet–clinopyroxene amphibolites from the metamorphic sole immediately beneath the Semail Thrust in Oman provided peak metamorphic conditions of 770–900 °C and 11–13 kb (Cowan et al., 2014). U–Pb zircon ages of *ca*. 96 and 94 Ma (Rioux et al., 2016) that date peak metamorphism of the sole overlap with crystallisation of the crustal section of the ophiolite at *ca*. 96.4–95.5 Ma (Rioux et al., 2013, 2012). Thus, it seems reasonable to assume that peridotites in the adjacent hanging-wall were deformed at similarly high temperatures.

While many studies have investigated the pressure, temperature, and deformation history of the metamorphic sole (e.g., Searle and Malpas, 1980, 1982; Hacker, 1990, 1994; Hacker and Mosenfelder, 1996; Gnos, 1998; Cowan et al., 2014; Rioux et al., 2016) and shear zones within the mantle section (e.g. Dijkstra and Drury, 2002; Michibayashi and Mainprice, 2004; Michibayashi et al., 2006; Linckens et al., 2011), relatively few have focused on the mylonitized peridotites along the base of the ophiolite. In a review of ophiolitic mantle sections, Nicolas et al. (1980) differentiate between an upper section with a coarse-grained porphyroclastic to granular texture, and a lower section with a fine-grained porphyroclastic to mylonitic texture. They interpret the upper peridotites as preserving high-temperature asthenospheric flow beneath an oceanic spreading centre, that is overprinted by the mylonitic and porphyroclastic textures related to lower-temperature thrusting during emplacement of the ophiolite. Boudier and Coleman (1981) conducted a microstructural analysis of peridotites from a

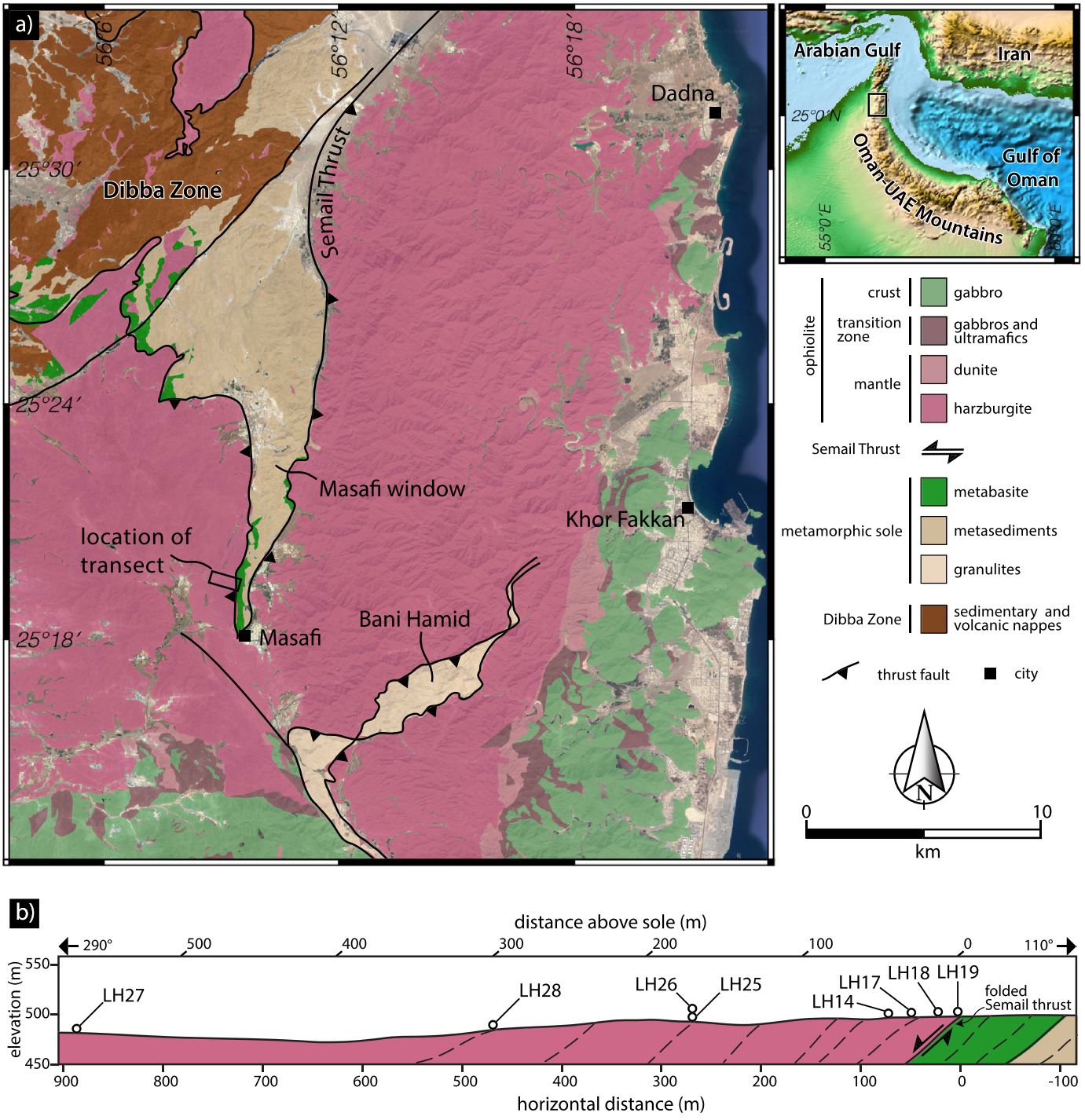

Fig. 1. (a) Simplified geological map of the northern United Arab Emirates (modified after Farrant et al., 2012) and elevation model showing the map location on the northeast margin of the Arabian peninsula. (b) Cross-section across the uppermost sole and basal peridotites with locations of analysed samples. Along the western margin of the Masafi window the Semail thrust has an apparent normal sense because the transport direction is to the west and the Semail thrust has been affected by later (post-emplacement) folding. Foliation is indicated by dashed lines. Distance above the sole was estimated using the average foliation of the upper sole and banding in peridotites, which approximate the orientation of the thrust contact. Horizontal distance is taken from the sole–peridotite contact. (For interpretation of the colours in the figure(s), the reader is referred to the web version of this article.)

~12 km transect across the mantle section of the ophiolite at Wadi Tayin, Oman. Olivine CPOs from this transect are characterised by [100] dominantly sub-parallel to the lineation and are interpreted to indicate slip on (010)[100] and {0kl}[100]. Boudier and Coleman (1981) additionally reported that the strength of the CPOs did not display any obvious trends with structural position. Subsequently, Boudier et al. (1988) mapped the distribution of fabrics related to either high-temperature asthenospheric flow or lower-temperature emplacement at several locations in Oman and the UAE. Unlike the previous study at Wadi Tayin, olivine CPOs weaken towards the sole and disappear in the basal mylonites (Boudier et al., 1988). In addition to harzburgite and dunite, which comprise the majority of the mantle sequence, several occurrences of lherzolite have also been described. Geochemical trends from the lherzolites have previously been interpreted to indicate some combination of melt extraction, interaction with a fluid or melt, and primary

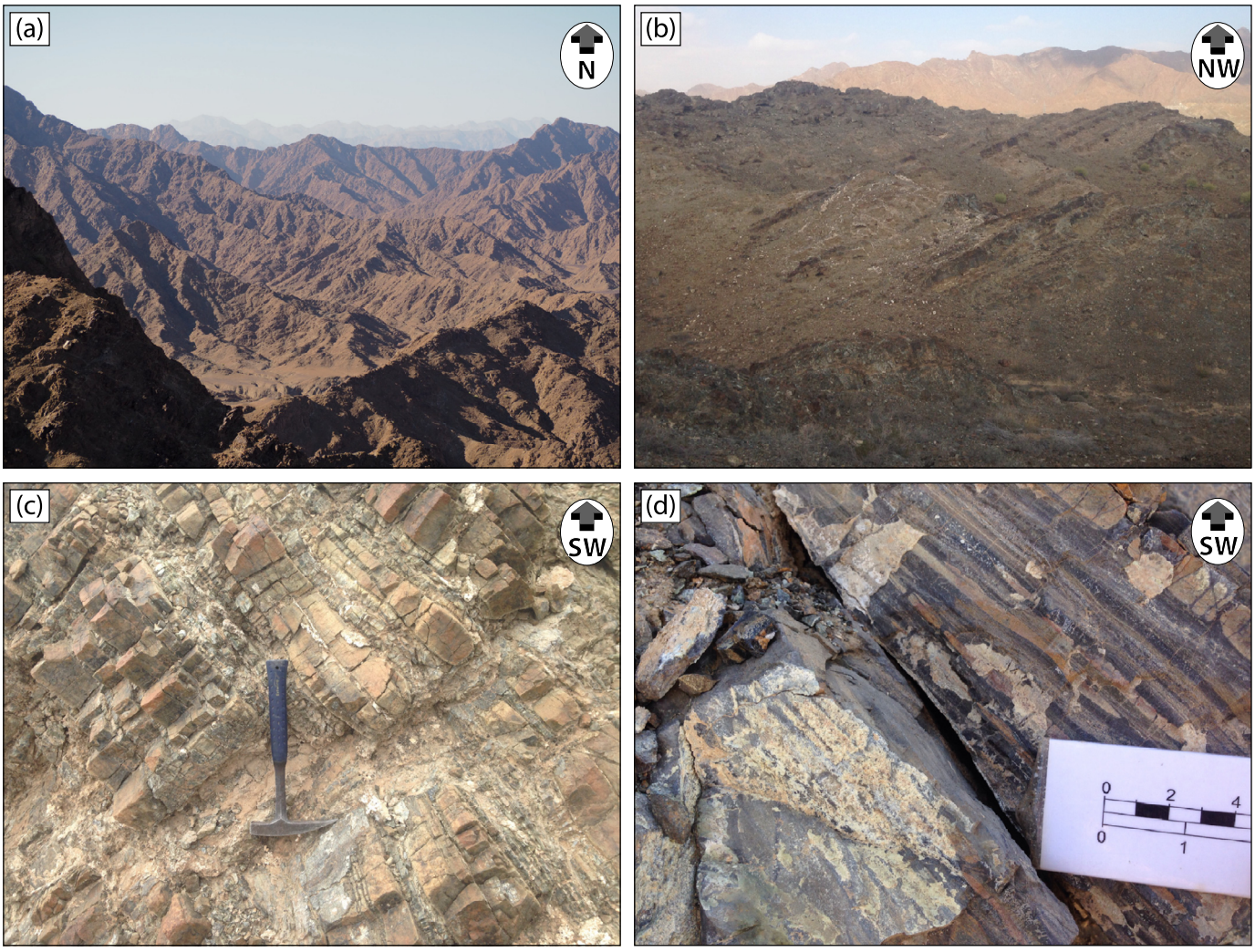

Fig. 2. Field photos of the Oman–UAE ophiolite mantle section. (a) Most of the mantle section lacks obvious lineations and foliation. (b)–(c) The basal kilometre of the mantle peridotites displays a foliation that increases in intensity towards the base. (d) The lowermost few metres of the ophiolite exhibit a well developed mylonitic fabric (Units on scale card are cm (top) and inches (bottom)).

mantle heterogeneity (Takazawa et al., 2003; Khedr et al., 2013; Yoshikawa et al., 2015).

3. Methods

3.1. Sample collection and preparation

The study area is located in the northern UAE where the ophiolite is folded and erosion has exposed the Semail thrust and underlying metamorphic sole in the Masafi window (Fig. 1). Eight oriented peridotite samples were collected along a ~900 m transect oriented perpendicular to the strike of the foliation of the peridotite and metamorphic sole (Fig. 1). The structurally lowest (easternmost) sample was located within a metre of the metamorphic sole. The transect spans a structural thickness of ~490 m in the direction normal to the mean orientation of foliation of the peridotite and metamorphic sole, which corresponds to a horizontal distance of nearly 900 m (Fig. 1b). As the strength and orientation of the foliation in the peridotites was variable and no lineation was observed, samples were cut with reference to the average orientation of foliation in the metamorphic sole (187°/39°), which is similar to the orientation of banding in the peridotite. Although a lineation was not observable in hand samples of peridotite or in amphibolites in the adjacent sole, a well-developed north-south trending mineral-stretching lineation that is parallel to fold-axes was observed in metasedimentary units further down the section in the metamorphic sole. Thin sections and billets were oriented perpendicular to orientation of the average foliation and parallel to the average dip direction. All analyses were on polished billets, aside from LH14 and LH19, which were performed on thin sections. All specimens were polished with progressively finer diamond slurry from 30 µm to 0.25 µm and finished with either 0.05 µm diamond or 0.03 µm colloidal silica.

3.2. Microstructural analysis

Mineral abundances, CPO, and grain sizes were quantified with electron backscatter diffraction (EBSD) data. These data were collected using an FEI Quanta 650 scanning electron microscope (SEM) with a field emission gun and an Oxford Instruments AZtec acquisition system and NordlysNano EBSD camera. Uncoated samples were mapped in low-vacuum mode (50 Pa) at 30 kV accelerating voltage with a step size of 5 µm (15 µm for LH19). Data were processed using Oxford Instruments Channel5 software and the MTEX toolbox (e.g., Hielscher and Schaeben, 2008) for MATLAB®. Channel5 was used to remove isolated pixels ('wildspikes'), and non-indexed points surrounded by ≥5 neighbours within the same grain were filled with the average of their neighbour orientations. After processing, ~10–80% of the map consisted of non-indexed pixels (Table 1), with increasing amount of non-indexing reflecting the degree of serpentinisation. Estimates of mean grain size and

Table 1
Results from EBSD analyses.

Sample	Position (m)	Modal abundances (%)							Olivine grain size (μm)	Minor phases grain size (μm)	Olivine subgrain size (μm)	Stress in olivine (MPa)	Olivine J-index
		Olivine	Cpx	Opx	Hbl	Sp	Non-indexed	Minor					
LH19	1	44	2.4	8.2	10	0.3	35	20.9	142	103			1.2
LH18	22	47	3.3	12	0.33	0.6	36	16.2	114	79	43.3	33.8	1.2
LH17	51	68	3.1	14	3.3	0.7	10	21.1	98	61	58.7	24.9	1.3
LH14	80	29	2.8	9		0.2	59	12.0	162	129	53.2	27.5	1.4
LH25	266	17	0.61	3.5	0.46	0.0	78	4.6	307	223			1.4
LH26	266	15	0.35	3.3	0.14	0.3	81	4.1	350	214			2.1
LH28	469	34	0.9	11	21	0.1	33	33.0	162	120	56.6	25.8	1.1
LH27	888	37	1.4	7.8	0.042	0.1	53	9.3	245	161	47.8	30.6	2.6

subgrain size were calculated in Channel5 using the line-intercept method (see Appendix A in Hansen et al., 2011). The method was applied parallel (X-direction) and perpendicular (Z-direction) to the foliation. Grain and subgrain boundaries were defined as having misorientation angles $>10°$ and 1–10°, respectively. A geometric correction factor of 1.5 was applied to convert mean intercept-length to estimates of mean grain size and mean subgrain size for use in flow laws (Underwood, 1970, pp. 80–93). For a material with significant regions of unindexed pixels, as is the case for some samples in this study, the line intercept method is better suited to determining (sub)grain sizes than methods based on grain area (Humphreys, 2001). Intercept lengths are measured with the line continuing uninterrupted, ignoring unindexed pixels (e.g., in a serpentine vein), until it reaches an indexed pixel with a misorientation angle relative to the last indexed pixel greater than the set threshold. This method may, however, overestimate the grain size in samples with high enough degrees of serpentinisation such that entire grains are missing.

EBSD data are used to estimate palaeostresses experienced by our samples. In monomineralic rocks, experimentally derived grain-size piezometers can be used to estimate differential stress (for olivine see: Karato et al., 1980; van der Wal et al., 1993). In polymineralic rocks, however, pinning due to minor phases may lead to overestimation of differential stress if grain size is maintained below that which would be attained in a monomineralic rock (Herwegh et al., 2011; Tasaka et al., 2014). Therefore, following the protocol outlined by Hansen and Warren (2015), we used the olivine subgrain-size piezometer of Toriumi (1979) to estimate differential stresses.

For each set of orientations, an orientation distribution function was determined using the automatic halfwidth algorithm in MTEX (Hielscher and Schaeben, 2008). Each orientation distribution function was calculated using one-point-per-grain for over 1000 grains. Unlike for grain-size measurements, grains were iteratively dilated in Channel5 using the orientation of adjacent pixels so that no non-indexed pixels remained. This minimised the likelihood of more than one point being included per grain due to grains being dissected by serpentine veins. Pole figures (i.e., graphical presentations of orientation distribution functions) are oriented in a geographic reference frame relative to the average foliation of the metamorphic sole (187°/39°) immediately beneath the ophiolite. All pole figures are plotted with the same colour-scale, as multiples of uniform distribution (M.U.D.) ranging from 0–2.5, to facilitate comparison among them. The strength of the CPO was quantified using the J-index (Bunge, 1982), which ranges from 1 for a uniform distribution of orientations to infinity for a single crystal.

3.3. Mineral abundances

Mineral abundances were calculated from the processed EBSD data using MTEX. Isolated porphyroclasts of orthopyroxene were excluded from modal abundance estimates as we are primarily interested in the volumetrically more significant matrix, which we assume controlled the rheological properties. Indexing ranged from ~20–90% and is primarily a reflection of the amount of serpentinisation. Most of the serpentinisation observed in the samples is interpreted to have resulted from surface processes, consistent with seismic velocities (Christensen and Smewing, 1981), as well as phase equilibria modelling, serpentine chemistry, and ∂O^{18} values for carbonate veins and ground water (Streit et al., 2012). Although pyroxenes can be serpentinised, olivine alters more rapidly (Wicks, 1969). As such, assuming that the other minerals were preserved and indexed, the non-indexed pixels are interpreted to have been primarily olivine prior to serpentinisation. Unindexed pixels are not included as a 'minor phase' in our analyses, but instead considered to be composed of olivine when calculating modal proportions.

4. Results

4.1. Petrography

Modal abundances of different mineral phases determined from EBSD maps are presented in Table 1. Olivine is the most abundant phase in all samples, even when only considering the indexed regions. Minor phases comprise 4–33% of the mapped regions, and consist primarily of orthopyroxene, with less abundant clinopyroxene, hornblende, and spinel (Table 1).

Examples of the spatial distribution of different mineral phases are presented as photomicrographs in Figs. 3a–c and EBSD maps in Figs. 4a–c (EBSD phase maps, band contrast maps, orientation maps, and local misorientation maps for all samples are provided in the supplementary data). Orthopyroxene occurs both as porphyroclasts (Figs. 3a, 4a, 4c) and as finer-grained material mixed within the matrix (Figs. 4b–c). Clinopyroxene occurs both as a fine-grained and well mixed phase throughout the matrix (Fig. 4b), as well as exsolution lamellae and inclusions within orthopyroxene (Fig. 4a). Hornblende is colourless in thin section and occurs both as a well-mixed, fine-grained phase in the matrix (Figs. 3b–c), as well as replacement rims around and within orthopyroxene (Figs. 4a and 4c). Several lines of evidence indicate that hornblende was present during high-temperature deformation, rather than having formed after deformation and/or at lower temperatures. First, hornblende is cut by serpentine veins and hence predates the low-temperature serpentinisation (Fig. 3b). Lizardite and chrysotile, the polymorphs of serpentine present in the ophiolite (e.g., Streit et al., 2012), are both unstable above about 400 °C (Evans, 2004), which places a minimum temperature limit for hornblende crystallisation. Second, hornblende exhibits lattice curvature indicative of crystal plasticity by dislocation motion (Fig. 4d), consistent with deformation temperatures in excess of 650–700 °C (Berger and Stünitz, 1996). Third, asymmetrical overgrowths of hornblende on orthopyroxene (Fig. 4c) indicate that deformation occurred in the stability field of hornblende, which does not overlap with that of serpentine.

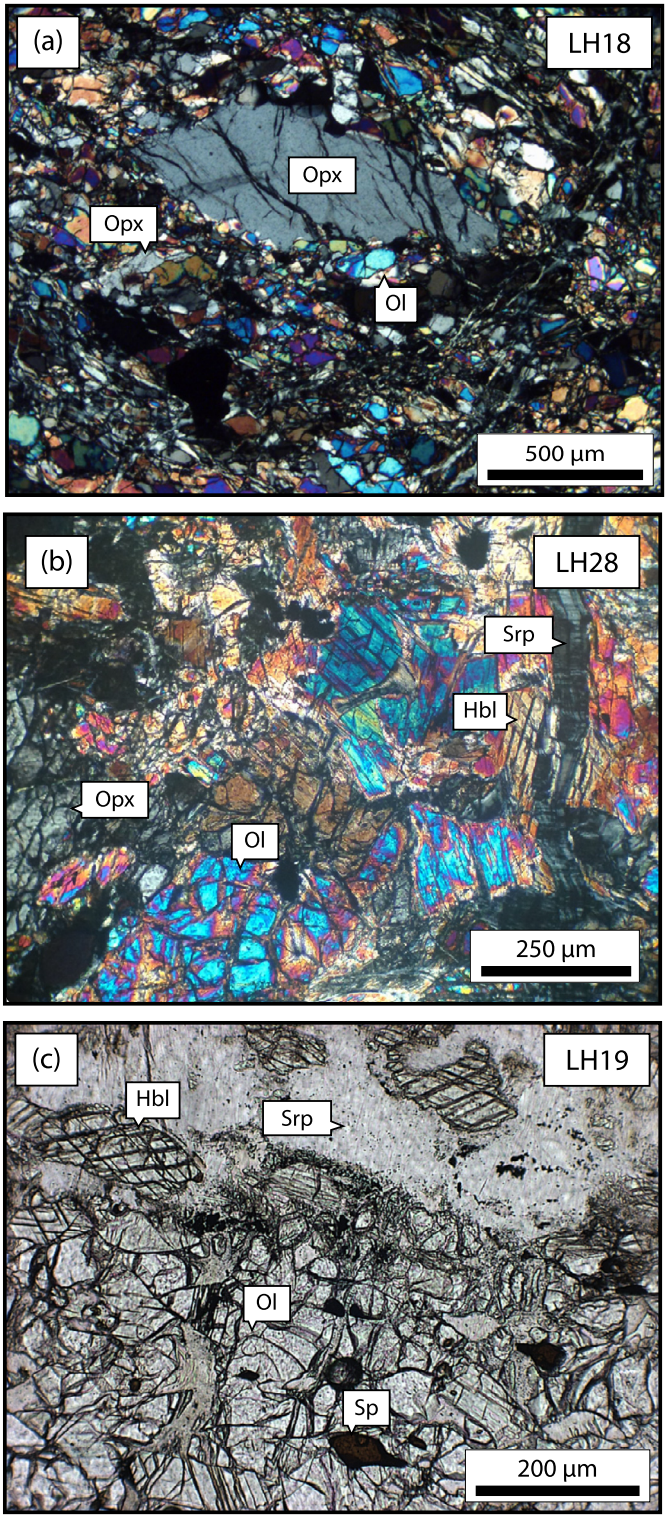

Fig. 3. Representative photomicrographs displaying: (a) an orthopyroxene porphyroclast surrounded by a fine-grained olivine matrix in sample LH18, (b) orthopyroxene, olivine, and hornblende cut by serpentine in sample LH28, and (c) olivine, hornblende, spinel, and serpentine in sample LH19. Ol (olivine), Opx (orthopyroxene), Cpx (clinopyroxene), Hbl (hornblende), Sp (spinel), Srp (serpentine).

4.2. Grain size and subgrain size

Fig. 5 presents distributions of intercept lengths used to estimate mean olivine grain size and mean olivine subgrain size. Estimates of the mean olivine grain sizes range from 98–350 µm (Fig. 5, Table 1). Three samples (LH19, LH25, LH26) were not sufficiently indexed to allow for an accurate estimate of the mean olivine subgrain size. Estimates of the mean olivine subgrain size of the remaining five samples range from 43–58 µm (Fig. 5, Table 1). The subgrain-size piezometer of Toriumi (1979) predicts corresponding differential stresses of 25–34 MPa. Estimates of the mean grain size of minor phases (excluding large and isolated porphyroclasts of orthopyroxene) range from 61–223 µm (Table 1).

4.3. Crystallographic preferred orientations

Olivine CPOs vary in strength but have similar shapes (Fig. 6). J-index values range from 1.1 for the weakest fabrics, to 2.6 for the strongest. Aside from LH28, all samples exhibit olivine CPOs characterised by [100] point maxima that are approximately parallel to the average foliation of the metamorphic sole, and [010] and [001] orientation distributions that range from diffuse girdles to point maxima approximately perpendicular to the average foliation of the metamorphic sole. The orientations of [100] point maxima are remarkably consistent across the transect, indicating a broadly similar deformation geometry throughout the sampled region. Furthermore, [100] point maxima are oriented roughly perpendicular to the dip direction and have a similar orientation to the mineral stretching lineation observed in the metamorphic sole (Fig. 6).

4.4. Microstructure as a function of position

Microstructural characteristics described above are presented as a function of position along the transect in Figs. 7a–d. Throughout this figure, sample LH28 is singled out with a red square because it exhibits an anomalously high proportion of minor phases that are primarily made up of hornblende. Mean olivine grain size generally decreases towards the sole (Fig. 7a). However, the mean olivine grain size in sample LH28 (red squares in Fig. 7) is only 162 µm, which is fine relative to adjacent samples. In contrast, mean olivine subgrain size, and hence stress estimates from subgrain-size piezometry (e.g., Toriumi, 1979), remain reasonably constant along the length of the transect (Fig. 7b).

Minor phases exhibit a linear increase in abundance towards the sole from about 260 m (Fig. 7c). Sample LH27, located furthest from the sole has a similar minor-phase content as the samples located at 266 m from the sole. However, sample LH28, collected 413 m from the sole, contains the highest minor-phase content of all samples, due primarily to the high hornblende content. If sample LH28 is ignored due to the anomalously high hornblende content, the minor phase fraction remains reasonably constant beyond 260 m (Fig. 7c).

The strength of the olivine CPO gradually decreases towards the sole, with J-index values of 2.6 furthest from the sole, and 1.2 immediately adjacent to the sole (Figs. 6 and 7d). Sample LH28 (red squares in Fig. 7d), however, has a weak CPO relative to adjacent samples and a J-index value of just 1.1, the lowest of any of the samples. Despite similar mineralogy, low degree of indexing (i.e., high degree of serpentinisation), and location along the transect, LH25 has a considerably weaker CPO than LH26, which was collected from the same location.

4.5. Relationships among grain size, minor-phase abundance, and texture strength

Although general trends can be observed with distance from the sole, there is significant covariance among microstructural characteristics. Fig. 7e demonstrates that mean olivine grain size and minor-phase abundance are inversely related. If sample LH28 (red squares) is ignored, the decrease in mean olivine grain size with increasing minor-phase content is roughly linear. In contrast,

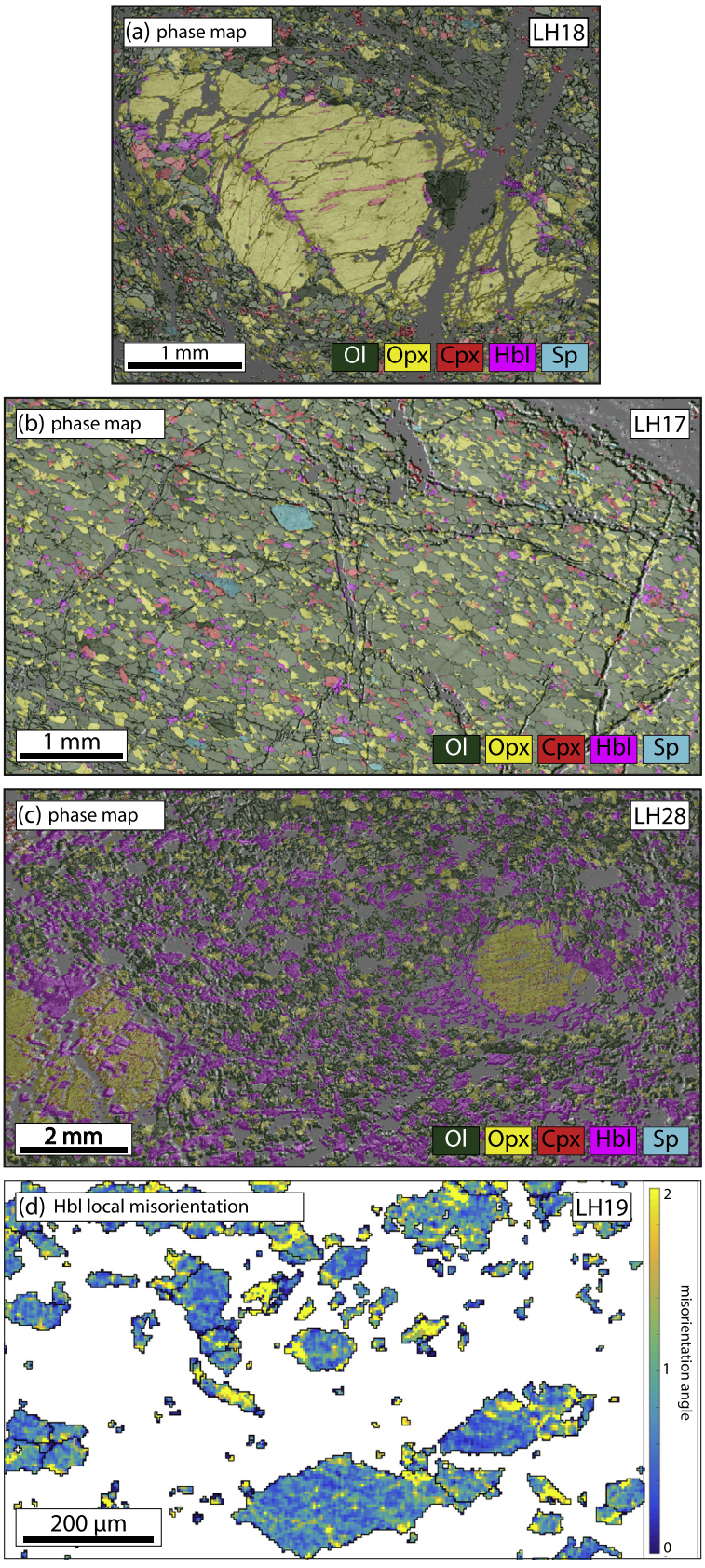

Fig. 4. EBSD maps. (a) Phase map overlain on band contrast map of sample LH18 displaying an orthopyroxene porphyroclast with clinopyroxene exsolution lamellae and hornblende replacement along fractures. Olivine appears to have penetrated and mixed with orthopyroxene along the bottom of the porphyroclast. (b) Phase map overlain on band contrast map of sample LH17 displaying olivine with well-mixed (dispersed) minor phases (orthopyroxene, clinopyroxene, and hornblende). (c) Phase map overlain on band contrast of map LH28 displaying porphyroclasts of orthopyroxene overgrown by hornblende and a finer-grained matrix of olivine, orthopyroxene, and hornblende. (d) Map of local misorientation in hornblende averaged within 3×3 pixel kernels. Abbreviations: Ol (olivine), Opx (orthopyroxene), Cpx (clinopyroxene), Hbl (hornblende), Sp (spinel). Gray pixels are mostly serpentine that was not indexed during EBSD analysis.

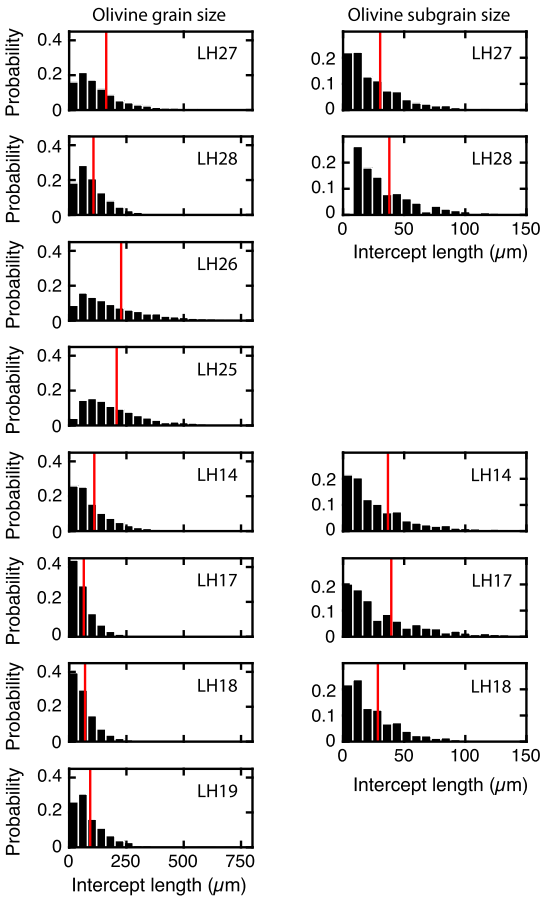

Fig. 5. Histograms of olivine grain size (left column) and subgrain size (right column) from intercepts measured parallel (x-direction) and perpendicular (z-direction) to foliation. Samples are ordered according to distance from the sole. The average grain sizes in Figs. 7, 8, and 9a, and Table 1 are an average of the *x*- and *z*-direction. A geometric correction factor of 1.5 was applied to convert intercept length to grain size.

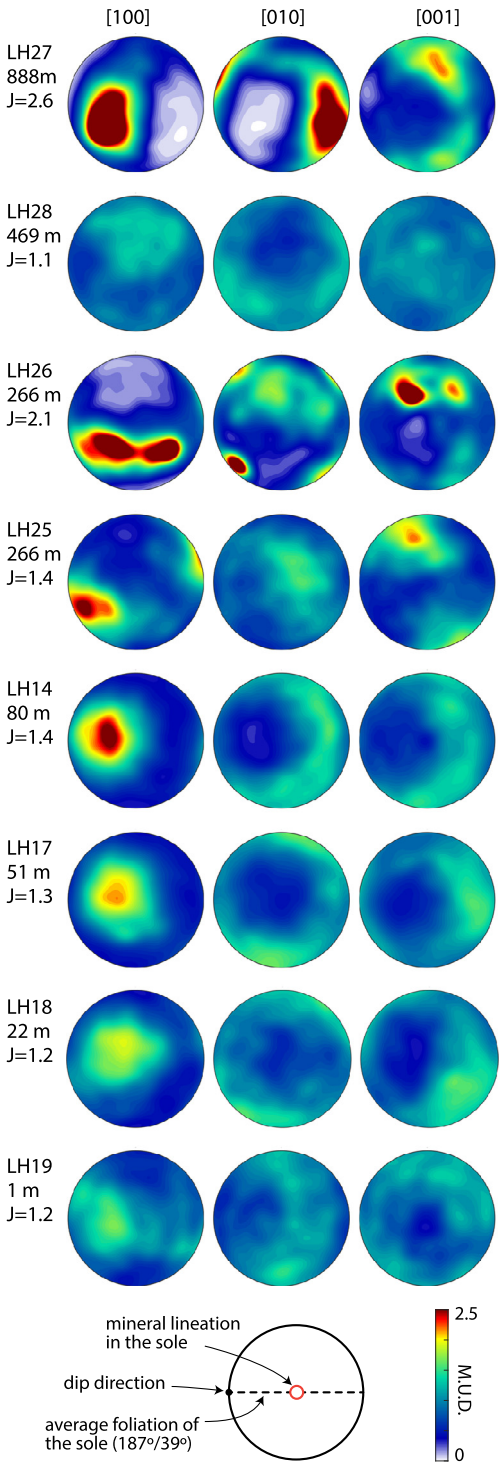

Fig. 6. Olivine pole figures for all samples illustrating the change in CPO from with distance from the sole. Distance from sole and J-index value are included for reference. Pole figures are oriented within a geographic reference frame, as schematically shown at the bottom. All figures are contoured for multiples of uniform distributions (M.U.D.) ranging from 0 to 2.5.

no relationship is evident between mean olivine subgrain size and minor-phase abundance (Fig. 7f).

Mean olivine grain size and texture strength exhibit a rough positive relationship (Fig. 7g). Samples with a mean olivine grain size less than 200 μm display reasonably constant and relatively low J-index values ranging from 1.1–1.4, whereas the three coarser samples exhibit a larger range but generally stronger texture strength, with J-index values between 1.4 and 2.6 (Fig. 7g). Sample LH28 has a somewhat weak texture strength relative to other samples with similar mean olivine grain sizes, but nonetheless is not an obvious outlier in Fig. 7g.

Minor-phase abundance and texture strength exhibit an inverse relationship (Fig. 7h). For minor-phase abundance below ~10%, there is a large range in the texture strength, with J-index values ranging from 1.4–2.6. However, for samples with a minor-phase abundance greater than ~10%, texture strength decreases linearly with minor-phase abundance with J-index values ranging from 1.4–1.1. In contrast to being an obvious outlier in Figs. 7a, 7c, 7d and 7e, sample LH28 lies along (albeit at the end) of the trend between texture strength and minor-phase abundance (Fig. 7g).

5. Discussion

5.1. Controls on strain localisation along the base of the Oman–UAE ophiolite

Studies of experimentally deformed rocks and outcrop-scale natural shear zones indicate that minor phases can control strain localisation (Farla et al., 2013; Hansen and Warren, 2015; Herwegh et al., 2011; Hiraga et al., 2010; Toy et al., 2010; Warren and Hirth, 2006; Tasaka et al., 2014, 2017). These small-scale studies are often used to infer the importance of minor phases in the formation of lithospheric-scale shear zones, and theoretical models have suggested that minor phases are crucial in the formation of tectonic plate boundaries (Bercovici and Ricard, 2014; Bercovici and Skemer, 2017). The Oman–UAE ophiolite provides a unique opportu-

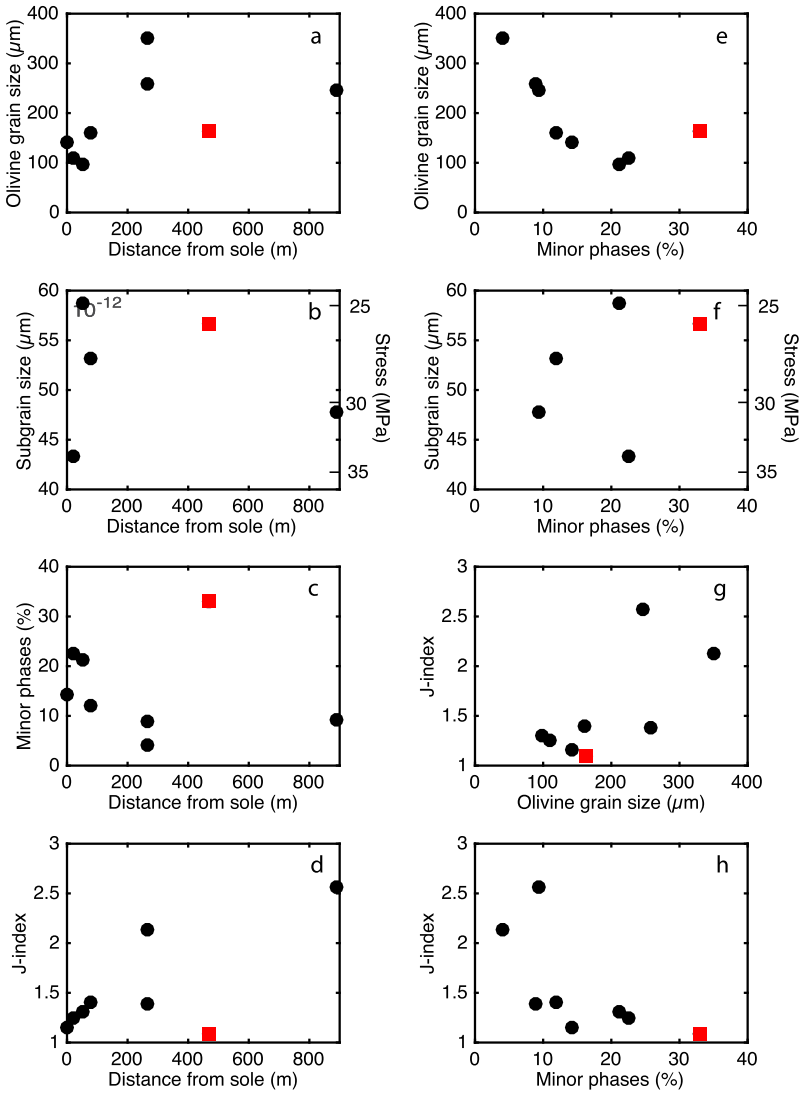

Fig. 7. Microstructural relationships. Subgrain sizes were not calculated for 3 samples due to insufficient indexing. In all plots, the red square corresponds to LH28.

nity to directly examine strain localisation at the larger and more relevant scale of a former plate boundary. In this section, we discuss the trends and relationships among minor-phase abundance, olivine grain size, and CPO strength from the mantle section at the base of the Oman–UAE ophiolite. As olivine is the most abundant and generally weakest phase in the upper mantle, it is often presumed to control the macroscopic rheology (Karato and Wu, 1993; Zimmerman and Kohlstedt, 2004). Furthermore, the recent experiments of Tasaka et al. (2013) demonstrate that, if olivine grain size is kept constant, even an increase in pyroxene fraction of 30% (roughly the maximum observed here) only modifies the macroscopic viscosity in diffusion creep by a factor of ~2 (see Fig. 10 in Tasaka et al., 2013). As presented below, this difference is insignificant compared to the changes in viscosity associated with changing the olivine grain size. The following discussion therefore focuses on olivine rheology, and in particular, the effect of minor-phases in moderating the strength of olivine.

5.2. The influence of minor phases on olivine grain size

Our results resolve an interplay between minor-phase content and olivine grain size along the base of the Oman ophiolite. Based on our initial observation in Fig. 7e, we suggest the inverse relationship between olivine grain size and minor-phase content is a result of minor phases pinning olivine grain boundaries. If true, our microstructural data should follow the general Zener equation, *olivine grain size* $= c \times$ *minor-phase grain size*/(*fraction of minor phases*)^m, where c is a constant of order 1 and m is a factor related to the spatial distribution of the dispersed phase (for reviews, see Evans et al., 2001; Herwegh et al., 2011). Based on theoretical development and computer simulation, $m$is predicted to take on values of 0.33 to 1. Fig. 8 presents our results using a value of $m = 0.52$, following the empirical determination by Tasaka et al. (2014) for olivine–pyroxene mixtures. Our data are consistent with this form of the Zener equation and in agreement with previous observations from natural peridotites (Linckens et al., 2011; Tasaka et al., 2013, 2014; Hansen and Warren, 2015), supporting our hypothesis that the presence of minor phases controlled olivine grain size along the base of the mantle wedge.

While the role of minor phases in limiting grain size is fairly well understood, the mechanism by which minor phases become mixed (i.e., dispersed) is still somewhat enigmatic. Hypotheses that have been proposed to explain mixing include nucleation of one phase in regions dominated by another phase as a result of stress-induced chemical potential gradients (Tasaka et al., 2017), nucleation of phases from a fluid in cavities opened by grain-boundary sliding (Precigout and Stüniz, 2016), or mechanical production of new grains that are transported along grain boundaries of an-

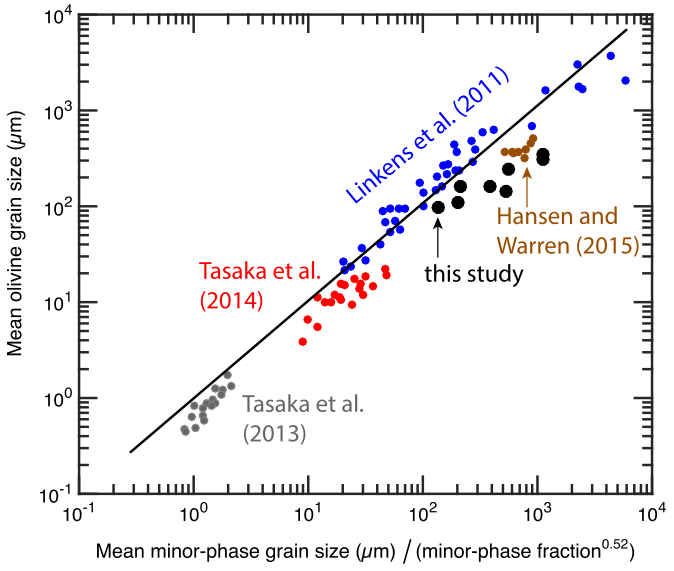

Fig. 8. Mean olivine grain size as a function of mean minor-phase grain size and minor-phase volume fraction. Following Tasaka et al. (2014), we use a value of $m = 0.52$ for the minor phase volume fraction. Our samples are plotted along with data from synthetic olivine–pyroxene aggregates (Tasaka et al., 2013), as well as data from natural shear zones in Oman (Linckens et al., 2011; Tasaka et al., 2014) and the Josephine peridotite (Hansen and Warren, 2015). The solid line is the best fit derived by Tasaka et al. (2014).

other phase as a result of surface tension and local stresses at the boundaries (Bercovici and Skemer, 2017). It is possible that multiple mechanisms were responsible for phase mixing in our samples. Clinopyroxene and hornblende, on the one hand, are interpreted to be produced from metasomatic fluids associated with the subducting slab (Prigent et al., 2014, 2015; Yoshikawa et al., 2015). Considering these phases are not generally seen as porphyroclasts and are primarily observed in well-mixed regions (Figs. 4b and c), it is possible they were generated by a mechanism similar to that proposed by Precigout and Stünitz (2016). Orthopyroxene, on the other hand, does occur as porphyroclasts, and small olivine grains appear to penetrate into the larger orthopyroxene grains (Fig. 4a). The location of these olivine grains does not appear to be controlled by orthopyroxene grain or subgrain boundaries, which is in better agreement with the model of Tasaka et al. (2017).

5.3. Deformation mechanisms and rheology of the subduction interface

We suggest that the grain-size reduction described above leads to weakening through a transition in deformation mechanism. We first use CPO strength to qualitatively assess variations in the relative contributions of dislocation creep and diffusion creep to the total strain rate. Deformation accommodated largely by the motion of dislocations typically leads to development of a CPO (e.g., Karato, 1988). In contrast, diffusion creep is presumed to produce a random or weak CPO (Fliervoet et al., 1999; Rutter et al., 1994). Although some questions remain regarding the effectiveness of diffusion creep in modifying an existing CPO (Wheeler, 2009), recent experiments on olivine–pyroxene mixtures by Tasaka et al. (2017) demonstrated that CPO strength decreases with increasing contributions of grain-size sensitive deformation to the strain rate. Therefore, the positive relationship between texture strength and mean olivine grain size in our samples (Fig. 7g) indicates that a mechanism other than dislocation creep was promoted by fine grain sizes. Given the influence of minor phases on olivine grain size (Figs. 7e and 8), this provides an explanation for the inverse correlation between minor-phase content and texture strength (Fig. 7h).

An increase in the fraction of strain produced by grain-size sensitive deformation at a given stress can result in rheological weakening and provide a mechanism for strain localisation (e.g., Drury, 2005; Warren and Hirth, 2006). To constrain the activity of different deformation mechanisms, we constructed deformation mechanism maps using the experimentally derived flow laws for wet olivine deforming by diffusion creep and dislocation creep as given by Hirth and Kohlstedt (2003; Fig. 9a). Hirth and Kohlstedt (2003) argued that dislocation-accommodated grain-boundary sliding (disGBS) is not important under hydrous conditions. Alternatively, Ohuchi et al. (2015) have more recently developed a flow law for disGBS in olivine under hydrous conditions based on high-pressure experiments. Their results, however, indicate that the contribution of disGBS to the total strain rate is insignificant at the deformation conditions expected along the base of the mantle wedge (low temperature and low stress). As such, we have not included disGBS in our calculations. Strain rates were calculated using a temperature of 800 °C and a confining pressure of 600 MPa. This pressure and temperature roughly correspond to peak temperature and intermediate pressure estimates from the hanging wall metamorphic sole (Cowan et al., 2014). The wet flow laws also include a term for hydrogen concentration (or water fugacity). Although the water content has not been precisely constrained in our dataset, the presence of hornblende is consistent with water-saturated conditions. At 800 °C and 600 MPa, the solubility of hydrogen in olivine is ~300 H/10^6 Si (Kohlstedt et al., 1996; Zhao et al., 2004). To assess the effect of water on strain rate, Figs. 9b and c present predicted strain rates using both the wet (Hirth and Kohlstedt, 2003) and dry (Hirth and Kohsltedt, 2003; Hansen et al., 2011) flow laws. Unlike the wet flow law of Hirth and Kohlstedt (2003), the dry flow laws of Hansen et al. (2011) and Hirth and Kohlstedt (2003) include a contribution from disGBS in addition to dislocation and diffusion creep. The wet flow law for water saturated olivine predicts an increase in strain rate of approximately two orders of magnitude relative to the dry flow laws (Fig. 9b). Importantly, the strain rate increases along the transect towards the sole, a feature that is apparent regardless of the water content used (Figs. 9b and c). Given the presence of hornblende, which suggests that significant amounts of water were present during deformation, and that the overall trends are not drastically affected by varying the water content, we have used a water concentration of 300 H/10^6Si in the flow laws for all samples (Fig. 9). It is worth noting, however, that the heterogeneous distribution of hornblende (Fig. 3) is consistent with channelised flow of a hydrous fluid (e.g. Plumper et al. 2016). Thus, it is possible that hydration of olivine varied along the section.

Our calculated deformation mechanism map is presented in Fig. 9a. The map is coloured by the fraction of the total strain rate due to dislocation creep to emphasise that the transition from dislocation creep to diffusion creep is gradational and does not reflect an abrupt 'switch' in deformation mechanism (e.g., Skemer and Hansen, 2016). Dislocation creep continues to operate at the same strain rates for a given stress in the diffusion creep field in stress-grain-size space. However, the proportion of the total strain rate due to dislocation creep decreases with decreasing grain size as the efficiency of diffusion creep increases. Our samples are plotted in Fig. 9a using measured olivine grain sizes and stress estimates from subgrain-size piezometry. All samples fall to the left of the nominal boundary between deformation mechanisms (50% diffusion creep and 50% dislocation creep). Aside from LH27, which was located furthest from the sole thrust, all of our samples are finer grained than predicted by grain-size piezometry (white dashed line; Van der Wal et al., 1993). The predicted percent of the total strain rate due to dislocation creep ranges from 3–46% and generally decreases towards the sole (Fig. 9d). Despite similar estimated stresses, this increase in diffusion creep is associated with an in-

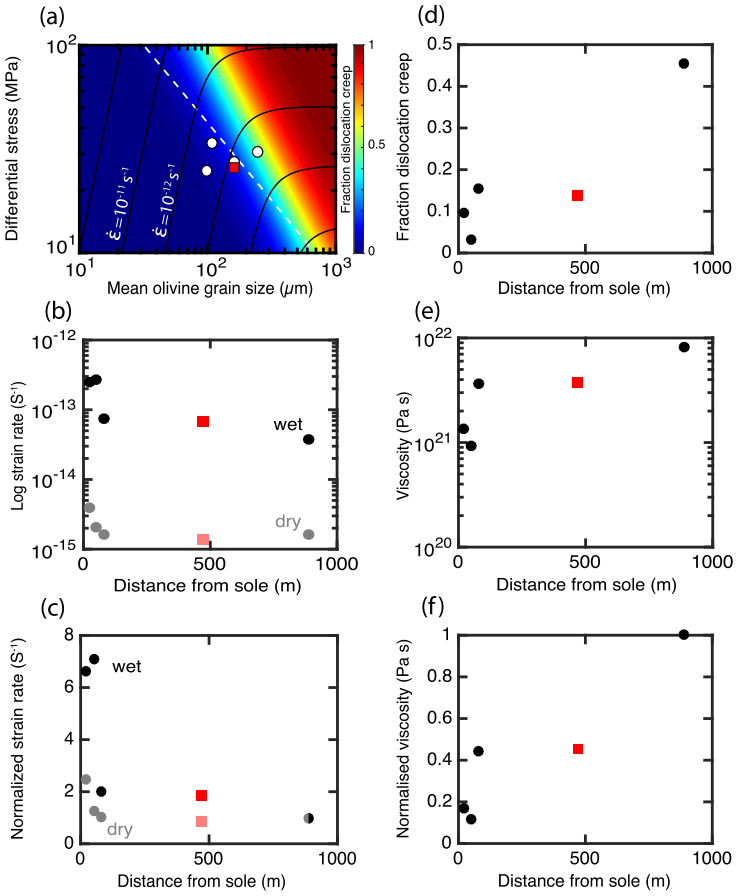

Fig. 9. (a) Deformation mechanism map for olivine using the wet flow laws for diffusion creep and dislocation creep (Hirth and Kohlstedt, 2003). Our samples are plotted using the measured grain size, and stress estimates from subgrain-size piezometry. The colour scale corresponds to the fraction of the total strain rate produced by dislocation creep. Flow laws were calculated using 800 °C, a confining pressure of 600 MPa, and 300 H/10^6Si. Black lines are contours for constant strain-rate. White dashed line is the grain-size piezometer of Van der Wal et al. (1993). (b) Predicted strain rates and (c) strain rates normalised to sample LH27 using the flow laws for wet olivine (black circles) and dry olivine (gray circles) as a function of distance from the sole. (d) Fraction of dislocation creep for wet olivine as a function of distance from the sole. (e) Predicted viscosities and (f) viscosities normalised to sample LH27 for wet olivine as a function of distance from the sole. Sample LH28 is displayed as a red square in all panels.

crease in predicted strain rates by a factor of ∼7.5 (4×10^{-14}–3×10^{-13} s^{-1}) towards the metamorphic sole (Figs. 9b and c). We also calculate that apparent viscosities decrease by a factor of ∼10 (10^{22}–10^{21} Pa s) within ∼100 m of the metamorphic sole (Figs. 9e and f).

Our estimated strain rates are reasonably consistent with geochronological constraints for both the ophiolite and metamorphic sole, as well as pressure estimates from the sole. Geochronology (Rioux et al., 2012, 2013, 2016) and thermochronology (Hacker, 1994) of the crustal sequence and metamorphic sole indicate that high-temperature deformation along the base of the ophiolite lasted approximately 1 Myr. The subducting slab reached depths of ∼40 km (Gnos, 1998; Cowan et al., 2014). For a dip of 45° and perpendicular convergence, these constraints correspond to ∼56 km of movement along the subduction interface and an upper bound for the strain rate of $\sim 10^{-12}$ s^{-1} for a 1 km wide shear zone.

The results from our microstructural analysis are consistent with the hypothesis that minor phases pinned olivine grain boundaries and limited grain-boundary migration, which hindered olivine grain growth and promoted diffusion creep. This transition in deformation mechanism had a weakening effect on olivine (Fig. 9a). As such, we suggest it was ultimately the distribution of minor phases that controlled the rheological weakening at the base of the mantle section. Similarly, Linckens et al. (2011) demonstrated a correlation between minor-phase abundance, grain size, and the rheological properties of peridotite from the vertical, strike-slip Hilti shear zone located within the middle of the mantle section in Oman. Here, we have demonstrated that minor phases also influenced strain localisation during subduction-related deformation along the base of the ophiolite. Our results are consistent with theoretical models that predict minor phases are necessary for the persistence of weak zones (i.e., plate boundaries) within the lithosphere (e.g., Berocovici and Ricard, 2012, 2014; Mulyukova and Bercovici, 2017).

Although generally stronger than olivine (e.g., Hansen and Warren, 2015), the net effect of increasing pyroxene content along our transect was a viscosity reduction. This conclusion is in contrast to the results of Hansen and Warren (2015). They examined a shear-zone formed under relatively dry conditions with a significant portion of the deformation occurring by disGBS. In the disGBS regime, they suggested the intrinsic strength of pyroxene roughly offsets any grain-size related weakening due to the relatively small grain-size sensitivity of disGBS. Thus, the hydrous conditions in the mantle section indirectly promoted significant weakening because diffusion creep is enhanced relative to disGBS (at this temperature and stress).

5.4. Orientation of CPOs and strain geometry at the subduction interface

For the deformation conditions expected along the subduction interface, it is expected that olivine would have [100] axes aligned approximately parallel to the transport direction (see Fig. 4 in Skemer and Hansen, 2016). However, Fig. 6 demonstrates that

olivine CPOs exhibit [100] axes at a high angle to the dip direction and more closely aligned with the stretching lineation in the metamorphic sole, particularly for the lower most sample. Four possible explanations can account for the difference between the orientation of the alignment of [100] axis and that of the dip direction. (1) It is possible that formation of the olivine CPOs predated deformation along the subduction interface. However, the high degree of olivine recrystallisation, systematic trends in the olivine CPO towards the metamorphic sole, orientation of the foliation parallel to the subduction interface, and evidence of deformation in the presence of hornblende all indicate that deformation and development of the CPO resulted from shearing along the subduction interface. (2) Another explanation is that the CPOs developed during high-stress and wet deformation conditions (Jung and Karato, 2001; Jung et al., 2006), which has been demonstrated to produce CPOs with [100] axes aligned perpendicular to the shear direction and the shear-plane normal (B-type fabric). However, the development of a B-type fabric requires significantly higher stresses than those estimated here by subgrain-size piezometery, even if the relatively low temperature of deformation is taken into account (Karato et al., 2008). (3) It is possible that the CPO developed during oblique convergence. However, the strain rates required to subduct the sole to 40 km in only 1 million years if subduction had a dominant strike-slip component are unrealistically high. Furthermore, thrusts, axial planes, and fold axes generally trend north-south, indicating that shortening was oriented east-west. (4) Our preferred explanation is that deformation was constrictional during (near) perpendicular convergence with a strong component of trench-parallel extension. Constrictional deformation is consistent with the well developed mineral stretching lineation in observed metasedimentary rocks in the metamorphic sole.

5.5. Tectonic implications

The role of minor phases in localising strain at the base of the mantle wedge has important implications for subduction zone processes. Theoretical models (e.g., Berocvici and Ricard, 2012, 2014; Mulyukova and Bercovici, 2017) have predicted that, by limiting grain growth and promoting grain-size sensitive deformation mechanisms, minor phases drive a positive self-weakening feedback that allows for the persistence of lithospheric weak zones. In particular, few geological processes are capable of reversing phase mixing. Thus, the presence and distribution of minor phases plays a critical role in the development and long-term maintenance of plate boundaries. Orthopyroxene was the most abundant minor phase in seven of eight samples in our transect. The large-scale spatial distribution of orthopyroxene is most easily explained by pre-existing mantle heterogeneity. In contrast, hornblende, the most abundant minor phase in one sample, and clinopyroxene have previously been interpreted to form during metasomatism of the mantle wedge by slab derived fluids (Prigent et al., 2015, 2014; Yoshikawa et al., 2015). Therefore, fluid transfer can yield additional localised weakening through crystallisation of minor phases that limit olivine grain growth and enhance diffusion creep. These fluids may additionally weaken the mantle through 1) the reduction of the crystal plastic strength of nominally anhydrous minerals, such as olivine, through incorporation of intracrystalline hydrogen (e.g., Mei and Kohlstedt, 2000a, 2000b) or 2) crystallisation of weaker phases such as serpentine and chlorite. Thus, weakening and localisation in the mantle near the subduction interface appears controlled by both pre-existing heterogeneity and infiltration of fluids from the slab.

In contrast to weakening of the mantle wedge, concomitant dehydration of the slab would have had a strengthening effect. The magnitude of the strengthening in the slab, however, is uncertain as there is a paucity of experimental data on the rheological influence of dehydration of metabasites. Fluid infiltration and amphibolitisation of gabbro (i.e., approximately the reverse reaction to that observed in the sole) has been demonstrated to have a significant weakening effect, primarily from the hydration of plagioclase (Getsinger et al., 2013).

The contrasting rheological evolution of the mantle wedge and downgoing slab has previously been proposed to control the progressive deepening of the subduction interface and associated accretion of slices of the downgoing slab (i.e., the future metamorphic sole) to the hanging-wall peridotites (e.g, Hacker, 1990; Agard et al., 2016). Agard et al. (2016) suggested that strain localizes where there is a large contrast in rheologies. In the model of Agard et al. (2016), the downgoing slab is initially stronger than the serpentinised mantle wedge and strain localizes at the interface between the two. However, with increasing depth and temperature the mantle wedge becomes less serpentinised and stronger, whereas the slab becomes hotter and weaker. At some critical point the downgoing slab and mantle wedge have similar viscosities and the locus of highest strain migrates into the slab. Here we have demonstrated that the abundance of minor phases exerts an additional and significant rheological control along the base of the mantle wedge not accounted for in previous models. Thus, dehydration and strengthening of the slab and concomitant metasomatism and weakening of the mantle wedge would enhance the strength contrast across the subduction interface, thereby limiting coupling to greater depths.

While our results demonstrate that the heterogeneous distribution of minor phases influences plate boundary development, they also raise questions as to the origin and extent of petrological heterogeneities in the mantle. Further insight would be gained by grid sampling (at the mm through to the km scale) across the mantle section of the ophiolite in bog-standard peridotite and characterising the distributions of grain size, composition, water, CPO, and modal mineral abundances on each scale.

6. Conclusions

Models of strain localisation at plate boundaries rely on the extrapolation of data from experimentally deformed rocks, small-scale natural shear zones, and shear zones in which the tectonic context is ambiguous. Direct observation of the strain localisation at plate boundaries is difficult due to the paucity of suitable exposure. We examined samples of peridotite collected across the base of the Oman–UAE ophiolite to elucidate the rheological controls on a palaeosubduction interface and use laboratory-based constraints to identify strain localisation.

Microstructural analyses reveal systematic changes in olivine grain size, minor-phase content, and olivine CPO. We demonstrate that minor phases pinned olivine grain boundaries and limited grain growth. The resultant finer grain size promoted diffusion creep and led to rheological weakening. We calculate that viscosity and strain rate respectively decrease and increase by approximately an order of magnitude towards the base of the ophiolite. Our data indicate that this rheological weakening was the result of more abundant minor phases near the base of the ophiolite. Orthopyroxene is the most abundant minor phase in all samples. The distribution of orthopyroxene is interpreted to reflect compositional heterogeneity that predates deformation. Unlike orthopyroxene, hornblende and clinopyroxene are interpreted to have crystallised during metasomatism of the mantle wedge by fluids from dehydration of the downgoing slab. Thus, in addition to hydrating and weakening olivine, metasomatic fluids released from the downgoing slab indirectly influenced strain localisation by promoting the crystallisation of minor phases that limited olivine grain size and promoted grain-size sensitive deformation mechanisms. Furthermore, based on our microstructural evidence and

recent laboratory deformation experiments, we suggest that the presence of a hydrous fluid promoted diffusion creep relative to disGBS, enhancing the grain-size sensitivity and associated weakening. While observed in experimentally deformed rocks and at the outcrop scale, this is the first demonstration that minor phases controlled strain localisation at a plate boundary. Moreover, our interpretations are consistent with theoretical models that suggest the distribution of minor phases strongly influence strain localisation along plate boundaries.

Acknowledgements

We are grateful to the Petroleum Institute for sponsoring this project (Project number: LTR14011). Tyler Ambrose thanks the Natural Sciences and Engineering Research Council (Canada) for supporting this project. David Wallis and Lars Hansen acknowledge support from the Natural Environment Research Council Grant NE/M000966/1. Comments from David Bercovici and two anonymous reviewers greatly enhanced this manuscript. We thank John Brodholt for his efficient editorial handling.

Appendix A. Supplementary material

Supplementary material related to this article can be found online at https://doi.org/10.1016/j.epsl.2018.03.027.

References

Agard, P., Yamato, P., Soret, M., Prigent, C., Guillot, S., Plunder, A., Dubacq, B., Chauvet, A., Monié, P., 2016. Subduction infancy: mantle resistance to slab penetration and metamorphic sole formation controlled by plate interface rheological switches. Earth Planet. Sci. Lett., 208–220. https://doi.org/10.1016/j.epsl.2016.06.054.

Austin, N., Evans, B., 2009. The kinetics of microstructural evolution during deformation of calcite. J. Geophys. Res., Solid Earth 114, 1–22. https://doi.org/10.1029/2008JB006138.

Bercovici, D., Karato, S., 2003. Theoretical Analysis of Shear Localization in the Lithosphere. Rev. Mineral. Geochemistry Plast. Deform. Miner. Rocks, vol. 51, pp. 387–421.

Bercovici, D., Ricard, Y., 2012. Mechanisms for lithospheric shear localization and the generation of plate tectonics by two-phase grain-damage and pinning. Phys. Earth Planet. Inter. 14, 12151. https://doi.org/10.1016/j.pepi.2012.05.003.

Bercovici, D., Ricard, Y., 2014. Plate tectonics, damage and inheritance. Nature 508, 513–516. https://doi.org/10.1038/nature13072.

Bercovici, D., Skemer, P., 2017. Grain damage, phase mixing and plate-boundary formation. J. Geodyn. 108, 40–55. https://doi.org/10.1016/j.jog.2017.05.002.

Berger, A., Stünitz, H., 1996. Deformation mechanisms and reaction of hornblende: examples from the Bergell tonalite (Central Alps). Tectonophysics 257, 149–174. https://doi.org/10.1016/0040-1951(95)00125-5.

Boudier, F., Coleman, R.G., 1981. Cross section through the peridotite in the Samail Ophiolite, southeastern Oman Mountains. J. Geophys. Res. 86, 2573. https://doi.org/10.1029/JB086iB04p02573.

Boudier, F., Ceuleneer, G., Nicolas, A., 1988. Shear zones, thrusts and related magmatism in the Oman ophiolite: initiation of thrusting on an oceanic ridge. Tectonophysics 151, 275–296. https://doi.org/10.1016/0040-1951(88)90249-1.

Bunge, H.-J., 1982. Texture Analysis in Materials Science: Mathematical Methods. Butterworth, London.

Christensen, N.I., Smewing, J.D., 1981. Geology and seismic structure of the Northern section of the Oman ophiolite. J. Geophys. Res. 86, 2545–2555.

Cowan, R.J., Searle, M.P., Waters, D.J., 2014. Structure of the metamorphic sole to the Oman Ophiolite, Sumeini Window and Wadi Tayyin: implications for ophiolite obduction processes. Geol. Soc. (Lond.) Spec. Publ. 392, 155–175. https://doi.org/10.1144/SP392.8.

Cross, A.J., Skemer, P., 2017. Ultramylonite generation via phase mixing in high strain experiments. J. Geophys. Res., 1–16. https://doi.org/10.1002/2016JB013801.

de Bresser, J.H.P., Peach, C.J., Reijs, J.P.J., Spiers, C.J., 1998. On dynamic recrystallization during solid state flow: effects of stress and temperature. Geophys. Res. Lett. 25, 3457–3460. https://doi.org/10.1029/98GL02690.

de Bresser, J.H.P., Ter Heege, J.H., Spiers, C.J., 2001. Grain size reduction by dynamic recrystallization: can it result in major rheological weakening? Int. J. Earth Sci. 90, 28–45. https://doi.org/10.1007/s005310000149.

Derby, B., Ashby, M.F., 1987. On dynamic recrystallisation. Scr. Metall. 21, 879–884. https://doi.org/10.1016/0036-9748(87)90341-3.

Dijkstra, A., Drury, M., 2002. Microstructures and lattice fabrics in the Hilti mantle section (Oman Ophiolite): evidence for shear localization and melt weakening in the crust–mantle transition zone? J. Geophys. Res. Earth 107, 2270. https://doi.org/10.1029/2001JB000458.

Drury, M., 2005. Dynamic recrystallization and strain softening of olivine aggregates in the laboratory and the lithosphere. Geol. Soc. (Lond.) Spec. Publ. 243, 143–158. https://doi.org/10.1144/GSL.SP.2005.243.01.11.

Evans, B.W., 2004. The serpentinite multisystem revisited: chrysotile is metastable. Int. Geol. Rev. 46, 479–506. https://doi.org/10.2747/0020-6814.46.6.479.

Evans, B., Renner, J., Hirth, G., 2001. A few remarks on the kinetics of static grain growth in rocks. Int. J. Earth Sci. 90, 88–103. https://doi.org/10.1007/s005310000150.

Farla, R.J.M., Karato, S.I., Cai, Z., 2013. Role of orthopyroxene in rheological weakening of the lithosphere via dynamic recrystallization. Proc. Natl. Acad. Sci. USA 110, 16355–16360. https://doi.org/10.1073/pnas.1218335110.

Farrant, A., Ellison, R.A., Thomas, R.J., Goodenough, K.M., Arkley, S.L.B., Burke, H.F., Carney, J.N., Finlayson, A., Jordan, C.J., Lee, J.R., Leslie, A.B., Merritt, J.E., Merritt, J., Newell, A.J., Phillips, E.R., Pickett, E.A. Price, S.J., Schofield, D.I., Smith, R., Stephenson, D., Styles, M.T., Warrak, M., 2012. Geological map of the United Arab Emirates. British Geological Survey, Keyworth, Nottingham.

Fliervoet, T.F., Drury, M., Chopra, P.N., 1999. Crystallographic preferred orientations and misorientations in some olivine rocks deformed by diffusion or dislocation creep. Tectonophysics 303, 1–27. https://doi.org/10.1016/S0040-1951(98)00250-9.

Getsinger, A.J., Hirth, G., Stünitz, H., Goergen, E.T., 2013. Influence of water on rheology and strain localization in the lower continental crust. Geochem. Geophys. Geosyst. 14, 2247–2264. https://doi.org/10.1002/ggge.20148.

Glennie, K.W., Boeuf, M.G.A., Hughes Clarke, M.W., Mood-Stuart, M., Pilaar, W.F.H., Reinhardt, B.M., 1973. Late Cretaceous nappes in Oman mountains and their geologic evolution. Am. Assoc. Pet. Geol. Bull. 57, 5–27. https://doi.org/10.1306/83D92032-16C7-11D7-8645000102C1865D.

Gnos, E., 1998. Peak metamorphic conditions of garnet amphibolites beneath the Semail ophiolite: implications for an inverted pressure gradient. Int. Geol. Rev. 40, 281–304. https://doi.org/10.1080/00206819809465210.

Hacker, B.R., 1990. Simulation of the metamorphic and deformational history of the metamorphic sole of the Oman ophiolite. J. Geophys. Res. Earth 95, 2527–2544. https://doi.org/10.1029/JB095iB04p04895.

Hacker, B.R., 1994. Rapid emplacement of young oceanic lithosphere: argon geochronology of the Oman ophiolite. Science 80 (265), 1563–1565. https://doi.org/10.1126/science.265.5178.1563.

Hacker, B.R., Mosenfelder, J.L., 1996. Metamorphism and deformation along the emplacement thrust of the Samail ophiolite, Oman. Earth Planet. Sci. Lett. 144, 435–451. https://doi.org/10.1016/S0012-821X(96)00186-0.

Hansen, L.N., Zimmerman, M.E., Kohlstedt, D.L., 2011. Grain boundary sliding in San Carlos olivine: flow law parameters and crystallographic-preferred orientation. J. Geophys. Res., Solid Earth 116, 1–16. https://doi.org/10.1029/2011JB008220.

Hansen, L.N., Warren, J.M., 2015. Quantifying the effect of pyroxene on deformation of peridotite in a natural shear zone. J. Geophys. Res., Solid Earth 120, 2717–2738. https://doi.org/10.1002/2014JB011584.

Herwegh, M., Linckens, J., Ebert, A., Berger, A.L., Brodhag, S.H., 2011. The role of second phases for controlling microstructural evolution in polymineralic rocks: a review. J. Struct. Geol. 33, 1728–1750. https://doi.org/10.1016/j.jsg.2011.08.011.

Hielscher, R., Schaeben, H., 2008. A novel pole figure inversion method: specification of the MTEX algorithm. J. Appl. Crystallogr. 41, 1024–1037. https://doi.org/10.1107/S0021889808030112.

Hiraga, T., Tachibana, C., Ohashi, N., Sano, S., 2010. Grain growth systematics for forsterite ± enstatite aggregates: effect of lithology on grain size in the upper mantle. Earth Planet. Sci. Lett. 291, 10–20. https://doi.org/10.1016/j.epsl.2009.12.026.

Hirth, G., Kohlstedt, D.L., 2003. Rheology of the upper mantle and the mantle wedge: a view from the experimentalists. In: Eiler, J.M. (Ed.), Inside the Subduction Factory. American Geophysical Union, pp. 83–105.

Humphreys, F.J., 2001. Grain and subgrain characterisation by electron backscatter diffraction. J. Mater. Sci. 36, 3833–3854. https://doi.org/10.1023/A:1017973432592.

Jung, H., Karato, S. Ichiro, 2001. Water-induced fabric transitions in olivine. Science 293, 1460–1463. https://doi.org/10.1126/science.1062235.

Jung, H., Katayama, I., Jiang, Z., Hiraga, T., Karato, S. Ichiro, 2006. Effect of water and stress on the lattice-preferred orientation of olivine. Tectonophysics 421, 1–22. https://doi.org/10.1016/j.tecto.2006.02.011.

Karato, S., Toriumi, M., Toshitsugu, F., 1980. Dynamic recrystallization of olivine single crystals during high-temperature creep. Geophys. Res. Lett. 7, 649–652.

Karato, S., 1988. The role of recrystallization in the preferred orientation of olivine. Phys. Earth Planet. Inter. 51, 107–122. https://doi.org/10.1016/0031-9201(88)90029-5.

Karato, S., Wu, P., 1993. Rheology of the upper mantle: a synthesis. Science 260, 771–778. https://doi.org/10.1126/science.260.5109.771.

Karato, S. Ichiro, Jung, H., Katayama, I., Skemer, P., 2008. Geodynamic significance of seismic anisotropy of the upper mantle: new insights from laboratory studies.

Annu. Rev. Earth Planet. Sci. 36, 59–95. https://doi.org/10.1146/annurev.earth.36.031207.124120.

Khedr, M.Z., Arai, S., Python, M., 2013. Petrology and chemistry of basal lherzolites above the metamorphic sole from Wadi Sarami central Oman ophiolite. J. Mineral. Petrol. Sci. 108, 13–24. https://doi.org/10.2465/jmps.121026.

Kohlstedt, D.L., Keppler, H., Rubie, D.C., 1996. Solubility of water in the α, β and γ phases of $(Mg, Fe)_2SiO_4$. Contrib. Mineral. Petrol. 123, 345–357. https://doi.org/10.1007/s004100050161.

Linckens, J., Herwegh, M., Muntener, O., Mercolli, I., 2011. Evolution of a polymineralic mantle shear zone and the role of second phases in the localization of deformation. J. Geophys. Res., Solid Earth 116, 1–21. https://doi.org/10.1029/2010JB008119.

MacLeod, C.J., Johan Lissenberg, C., Bibby, L.E., 2013. "Moist MORB" axial magmatism in the Oman ophiolite: the evidence against a mid-ocean ridge origin. Geology 41, 459–462. https://doi.org/10.1130/G33904.1.

Mei, S., Kohlstedt, D.L., 2000a. Influence of water on plastic deformation of olivine aggregates 1. Diffusion creep regime. J. Geophys. Res. 105, 21456–21469.

Mei, S., Kohlstedt, D.L., 2000b. Influence of water on plastic deformation of olivine aggregates 2. Dislocation creep regime. J. Geophys. Res. 105, 21471–21481. https://doi.org/10.1029/2000jb900180.

Michibayashi, K., Ina, T., Kanagawa, K., 2006. The effect of dynamic recrystallization on olivine fabric and seismic anisotropy: insight from a ductile shear zone, Oman ophiolite. Earth Planet. Sci. Lett. 244, 695–708. https://doi.org/10.1016/j.epsl.2006.02.019.

Michibayashi, K., Mainprice, D., 2004. The role of pre-existing mechanical anisotropy on shear zone development within oceanic mantle lithosphere: an example from the Oman ophiolite. J. Petrol. 45, 405–414. https://doi.org/10.1093/petrology/egg099.

Mulyukova, E., Bercovici, D., 2017. Formation of lithospheric shear zones: effect of temperature on two-phase grain damage. Phys. Earth Planet. Inter. 270, 195–212. https://doi.org/10.1016/j.pepi.2017.07.011.

Nicolas, A., Boudier, F., Bouchez, J.-L., 1980. Interpretation of peridotite structures from ophiolitic and oceanic environments. Am. J. Sci.

Ohuchi, T., Kawazoe, T., Higo, Y., Funakoshi, K.-I., Suzuki, A., Kikegawa, T., Irifune, T., 2015. Dislocation-accommodated grain boundary sliding as the major deformation mechanism of olivine in the Earth's upper mantle. Sci. Adv. 1, e1500360. https://doi.org/10.1126/sciadv.1500360.

Pearce, J.A., Alabaster, T., Shelton, A.W., Searle, M.P., 1981. The Oman ophiolite as a Cretaceous arc-basin complex: evidence and implications. Philos. Trans. R. Soc. Lond. 300, 299–317. https://doi.org/10.1098/rsta.1981.0066.

Plümper, O., John, T., Podladchikov, Y.Y., Vrijmoed, J.C., Scambelluri, M., 2016. Fluid escape from subduction zones controlled by channel-forming reactive porosity. Nat. Geosci. 1. https://doi.org/10.1038/NGEO2865.

Poirier, J.P., Guillopé, M., 1979. Deformation induced recrystallization of minerals. Bull. Miner. 102, 67–74.

Précigout, J., Stünitz, H., 2016. Evidence of phase nucleation during olivine diffusion creep: a new perspective for mantle strain localisation. Earth Planet. Sci. Lett. 455, 94–105. https://doi.org/10.1016/j.epsl.2016.09.029.

Prigent, C., Guillot, S., Agard, P., Godard, M., 2015. Mantle wedge formation during subduction initiation: evidence from the refertilized base of the Oman ophiolitic mantle. In: EGU Abstracts.

Prigent, C., Guillot, S., Agard, P., Godard, M., Chauvet, A., 2014. The basal part of the Oman ophiolitic mantle: a fossil Mantle Wedge? In: EGU Abstracts, p. 10266.

Rioux, M., Bowring, S., Kelemen, P.B., Gordon, S., Dudás, F., Miller, R., 2012. Rapid crustal accretion and magma assimilation in the Oman-U.A.E. ophiolite: high precision U–Pb zircon geochronology of the gabbroic crust. J. Geophys. Res. 117, B07201. https://doi.org/10.1029/2012JB009273.

Rioux, M., Bowring, S., Kelemen, P.B., Gordon, S., Miller, R., Dudás, F., 2013. Tectonic development of the Samail ophiolite: high-precision U–Pb zircon geochronology and Sm–Nd isotopic constraints on crustal growth and emplacement. J. Geophys. Res., Solid Earth 118, 2085–2101. https://doi.org/10.1002/jgrb.50139.

Rioux, M., Garber, J., Bauer, A., Bowring, S., Searle, M.P., Kelemen, P.B., Hacker, B.R., 2016. Synchronous formation of the metamorphic sole and igneous crust of the Semail ophiolite: new constraints on the tectonic evolution during ophiolite formation from high-precision U–Pb zircon geochronology. Earth Planet. Sci. Lett. 451, 185–195. https://doi.org/10.1016/j.epsl.2016.06.051.

Rutter, E.H., Brodie, K.H., 1988. The role of tectonic grain size reduction in the rheological stratification of the lithosphere. Geol. Rundsch. 77, 295–307. https://doi.org/10.1007/BF01848691.

Rutter, E.H., Casey, M., Burlini, L., 1994. Preferred crystallographic orientation development during the plastic and superplastic flow of calcite rocks. J. Struct. Geol. 16, 1431–1446. https://doi.org/10.1016/0191-8141(94)90007-8.

Searle, M.P., Malpas, J., 1980. Structure and metamorphism of rocks beneath the Semail ophiolite of Oman and their significance in ophiolite obduction. Trans. R. Soc. Edinb. Earth Sci. 71, 247–262. https://doi.org/10.1017/S0263593300013614.

Searle, M.P., Malpas, J., 1982. Petrochemistry and origin of sub-ophiolitic metamorphic and related rocks in the Oman Mountains. Mem. Geol. Soc. Lond. 139, 235–248. https://doi.org/10.1144/gsjgs.139.3.0235.

Searle, M.P., 1988. Thrust tectonics of the Dibba zone and the structural evolution of the Arabian continental margin along the Musandam mountains (Oman and United Arab Emirates). Mem. Geol. Soc. Lond. 145, 43–53. https://doi.org/10.1144/gsjgs.145.1.0043.

Skemer, P., Hansen, L.N., 2016. Inferring upper-mantle flow from seismic anisotropy: an experimental perspective. Tectonophysics 668–669, 1–14. https://doi.org/10.1016/j.tecto.2015.12.003s.

Streit, E., Kelemen, P.B., Eiler, J., 2012. Coexisting serpentine and quartz from carbonate-bearing serpentinized peridotite in the Samail Ophiolite, Oman. Contrib. Mineral. Petrol. 164, 821–837. https://doi.org/10.1007/s00410-012-0775-z.

Tackley, P.J., 2000. The quest for self-consistent generation of plate tectonics in mantle convection models. In: Richards, M.A., Gordon, R., van der Hilst, R. (Eds.), The History and Dynamics of Global Plate Motions. In: American Geophysical Union Monograph, vol. 121. American Geophysical Union, Washington, DC, pp. 47–72.

Takazawa, E., Okayasu, T., Satoh, K., 2003. Geochemistry and origin of the basal lherzolites from the northern Oman ophiolite (northern Fizh block). Geochem. Geophys. Geosyst. 4. https://doi.org/10.1029/2001GC000232.

Tasaka, M., Hiraga, T., Zimmerman, M.E., 2013. Influence of mineral fraction on the rheological properties of forsterite + enstatite during grain-size-sensitive creep: 2. Deformation experiments. J. Geophys. Res., Solid Earth 118, 3991–4012. https://doi.org/10.1002/jgrb.50284.

Tasaka, M., Hiraga, T., Michibayashi, K., 2014. Influence of mineral fraction on the rheological properties of forsterite + enstatite during grain size sensitive creep: 3. Application of grain growth and flow laws on peridotite ultramylonite. J. Geophys. Res., Solid Earth 119, 840–857. https://doi.org/10.1002/2013JB010619.

Tasaka, M., Zimmerman, M.E., Kohlstedt, D.L., Stünitz, H., Heilbronner, R., 2017. Rheological weakening of olivine + orthopyroxene aggregates due to phase mixing, Part 2: microstructural development. J. Geophys. Res., Solid Earth 122, 7597–7612. https://doi.org/10.1002/2017JB014311.

Toriumi, M., 1979. Relation between dislocation density and subgrain size of naturally deformed olivine in peridotites. Contrib. Mineral. Petrol. 68, 181–186. https://doi.org/10.1007/BF00371899.

Toy, V.G., Newman, J., Lamb, W., Tikoff, B., 2010. The role of pyroxenites in formation of shear instabilities in the mantle: evidence from an ultramafic ultramylonite, Twin Sisters massif, Washington. J. Petrol. 51, 55–80. https://doi.org/10.1093/petrology/egp059.

Underwood, E., 1970. The Mathematical Foundations of Quantitative Stereology, Quantitative Stereology. Addison-Wesley, Reading, MA.

Van der Wal, D., Chopra, P., Drury, M., Fitz Gerald, J., 1993. Relationships between dynamically recrystallized grain size and deformation conditions in experimentally deformed olivine rocks. Geophys. Res. Lett. 20, 1479–1482. https://doi.org/10.1029/93GL01382.

Warren, C.J., Parrish, R.R., Waters, D.J., Searle, M.P., 2005. Dating the geologic history of Oman's Semail ophiolite: insights from U–Pb geochronology. Contrib. Mineral. Petrol. 150, 403–422. https://doi.org/10.1007/s00410-005-0028-5.

Warren, J.M., Hirth, G., 2006. Grain size sensitive deformation mechanisms in naturally deformed peridotites. Earth Planet. Sci. Lett. 248, 423–435. https://doi.org/10.1016/j.epsl.2006.06.006.

Wheeler, J., 2009. The preservation of seismic anisotropy in the Earth's mantle during diffusion creep. Geophys. J. Int. 178, 1723–1732. https://doi.org/10.1111/j.1365-246X.2009.04241.x.

Wicks, F.J., 1969. X-Ray and Optical Studies of Serpentine Minerals. DPhil Thesis. University of Oxford.

Yoshikawa, M., Python, M., Tamura, A., Arai, S., Takazawa, E., Shibata, T., Ueda, A., Sato, T., 2015. Melt extraction and metasomatism recorded in basal peridotites above the metamorphic sole of the northern Fizh massif, Oman ophiolite. Tectonophysics 650, 53–64. https://doi.org/10.1016/j.tecto.2014.12.004.

Zhao, Y.H., Ginsberg, S.B., Kohlstedt, D.L., 2004. Solubility of hydrogen in olivine: dependence on temperature and iron content. Contrib. Mineral. Petrol. 147, 155–161. https://doi.org/10.1007/s00410-003-0524-4.

Zimmerman, M.E., Kohlstedt, D.L., 2004. Rheological properties of partially molten lherzolite. J. Petrol. 45, 275–298. https://doi.org/10.1093/petrology/egg089.